Angewandte Chemie International Edition

Angewandte International Edition Chemie

GDCh German Chemical Society

How to cite: *Angew. Chem. Int. Ed.* **2026**, e4468525
doi.org/10.1002/anie.4468525

RESEARCH ARTICLE

Spin Channels Enable •H-Triggered Ozone Activation for Self-Accelerating Degradation of Reduced-Sulfur Pollutant

Rumeng Zhang[1,2] | Shulin Zuo[1,2] | Mengliang Hu[3] | Ji Mei[1,2] | Keyu Chen[1,2] | Zhenxi Yuan[1,2] | Dehua Xia[1,2]

[1]School of Environmental Science and Engineering, Sun Yat-Sen University, Guangzhou510275, P.R. China | [2]Guangdong Provincial Key Laboratory of Environmental Pollution Control and Remediation Technology, Sun Yat-Sen University, Guangzhou510275, P.R. China | [3]School of Materials, Sun Yat-Sen University, Shenzhen518107, P.R. China

Correspondence: Dehua Xia (xiadehua3@mail.sysu.edu.cn)

Received: 2 December 2025 | **Revised:** 17 February 2026 | **Accepted:** 28 February 2026

Keywords: hydrogen radical (•H) | methanethiol (CH_3SH) | ozone activation | spin channels | volatile organic compounds (VOCs)

ABSTRACT

The practical application of catalytic ozonation for sulfurous volatile organic compounds (S-VOCs) is limited by two key challenges: sluggish electron transfer in ozone activation and irreversible catalyst deactivation from sulfur poisoning. Here, we report a strategy to overcome the "activation–poisoning" cycle through the engineering of $Cu_xMn_{3-x}O_4$ spinels, which repurpose CH_3SH from a poison into a co-catalyst, triggering self-accelerating degradation. The optimized $Cu_{0.75}Mn_{2.25}O_4$ demonstrated exceptional stability with complete CH_3SH mineralization over 28 h, sharply contrast to the rapid deactivation of Mn_3O_4. Mechanistic studies reveal that this enhancement originates from hydrogen radical (•H)-triggered chain reaction: Cu sites selectively mediate S—H homolysis to generate •H, which directly reduces O_3 at Mn sites, driving rapid hydroxyl radical (•OH) formation. This •H-mediated O_3 activation is enabled by spin-polarized electron transfer along Cu—O—Mn spin channels, where Cu doping enhances the O 2p—Mn 3d hybridization, builds delocalized electron pathways, and sustains Cu^{2+}/Cu^{+} and Mn^{4+}/Mn^{3+} redox cycling. Instantaneous •H consumption prevents sulfur intermediates accumulation and poisoning. This work transforms catalyst poisoning into a pollutant-driven, self-accelerating process via engineered spin-polarized channels, offering a design strategy for anti-poisoning environmental catalysts and advancing sustainable S-VOC abatement.

1 | Introduction

Reduced-sulfur volatile organic compounds (S-VOCs), a major class of toxic and malodorous air pollutants from industrial and biogenic sources, are key precursors to SO_2 and sulfate upon atmospheric oxidation, significantly contributing to fine-particle formation and acid deposition [1, 2]. Among them, methanethiol (CH_3SH) is a prototypical S-VOC with an extremely low human odor detection threshold of 1.6 ppb, causing nuisance at trace levels [3]. In the atmosphere it is readily oxidized to SO_2 and then to sulfate, further aggravating air-quality and health/odor management challenges [4–7]. Catalytic ozonation is an attractive end-of-pipe technology for reduced-sulfur VOC abatement as it enables deep mineralization at ambient–low temperatures: ozone (E_0 = 2.07 V) can react via selective molecular-O_3 pathways or, on suitable surfaces, be converted to coordinated reactive oxygen (predominantly •OH radicals) capable of cleaving the C—S bond (bond energy: 338 kJ mol^{-1})—the core step for CH_3SH mineralization [8–11]. However, practical implementation of this technology has long been constrained by two persistent bottlenecks: (i) O_3 activation is kinetically limited by sluggish catalyst-mediated electron transfer [12]; and (ii) sulfur-containing intermediates readily induce irreversible sulfur poisoning and catalyst deactivation [13, 14]. The prevailing research paradigm prioritizes maximizing O_3 activation while treating the pollutant as an unavoidable poison,

thereby locking the process into a passive "activation–poisoning" cycle.

Recently, an emerging paradigm in catalysis has challenged this conventional view: adsorbed pollutants do not merely deactivate catalysts but act as active participants in the catalytic cycles. For example, Huang and co-workers demonstrated that CuO activates adsorbed phenols via ligand-to-metal charge transfer (LMCT), generating phenoxyl radicals that drive a self-accelerated Fenton (SAHF) process [15, 16]. Similarly, enzyme-inspired catalytic membranes harness pollutant-derived electrons to sustain redox cycles for autonomous oxygen activation [17]; FeCo dual-single-atom catalysts enable oxidant-free pollutant degradation by leveraging contaminants as electron donors to modulate active-site electronic structures [18], while proton transfer-induced in situ formation of C═N sites from low-carbon amines triggers autocatalytic peroxymonosulfate (PMS) activation [19]. Even precious metals in e-waste can autocatalytically activate PMS via self-generated reactive species [20]. Collectively, these studies underscore a pivotal design principle: by steering pollutant adsorption to tailored sites and coupling it with efficient charge-transfer or radical-generation pathways, contaminants can be transformed from passive poisons into active co-activators.

Moving beyond the conventional focus solely on O_3 activation, we turn to spinel oxides (AB_2O_4) to simultaneously tackle the bottlenecks in S-VOC ozonation and harness this pollutant-involved activation paradigm. Leveraging their structural stability and tunable cation sublattices, we focus on Mn-based spinels for their rich $Mn^{2+}/Mn^{3+}/Mn^{4+}$ redox activity [21, 22]. According to crystal field theory, electron transfer in spinels proceeds along lattice oxygen-bridged A—O—B pathways between distinct metal ions in tetrahedral (A) and octahedral (B) sites. However, in hausmannite Mn_3O_4, the specific configuration of Mn^{2+} (Td) and high-spin Mn^{3+} (Oh) leads to limited orbital overlap and pronounced Jahn–Teller distortion. This results in localized e_g electrons and intrinsically sluggish intersite charge transfer.

This study thus adopts a dual-functional design by introducing Cu^{2+} ($3d^9$) into Mn_3O_4. On one hand, prior work has demonstrated that Cu 3d—O 2p interactions strongly redistribute M—O bond electron density, enhance lattice-oxygen reactivity, and synergize with Mn^{3+} ($3d^4$) to lower electron transfer barriers in A-O-B channels laying a robust structural foundation for enhanced O_3 activation [23–25]. On the other hand, building on our group's previous findings, Cu sites exhibit specific coordinative affinity toward sulfur-containing compounds: the empty $d_{x^2-y^2}$ orbital of Cu^{2+} forms stable Cu—S bonds with the lone pair electrons (3p orbital) of S in CH_3SH [26, 27]. We hypothesize that Cu doping not only strengthens CH_3SH pre-adsorption but also steers it toward specific sites, reducing its competition with O_3 for Mn active sites and fundamentally circumventing poisoning risks. Accordingly, we designed the $Cu_xMn_{3-x}O_4$ catalyst series.

Systematic evaluation of the $Cu_xMn_{3-x}O_4$ catalysts uncovered a striking phenomenon that runs counter to the conventional sulfur poisoning notions: on the Cu-optimized spinel, adsorbed CH_3SH did not poison the catalyst but instead dramatically boosted O_3 activation and degradation, exhibiting remarkable self-accelerating kinetics. This deviates sharply from the traditional Langmuir–Hinshelwood (L–H) mechanism based on competitive adsorption, signaling a hitherto unrecognized reaction pathway in which CH_3SH may transition from a "substrate to be degraded" to a "co-activator" of the catalytic reaction. To decipher this counterintuitive behavior, mechanistic investigations revealed that Cu sites serve as a directional "initiator" of the reaction. Specifically, they catalyze the homolytic cleavage of the S—H bond in CH_3SH to generate •H—a strongly reducing species (E_0 = −2.1 V) that directly triggers O_3 reduction at Mn sites, markedly lowering the O—O bond cleavage energy barrier. Furthermore, facilitated by efficient electron transfer across the Cu—O—Mn bridge, this rapid charge delivery synergistically enables the burst generation of •OH. This cascade mechanism—where •H generation at Cu sites couples with O_3 activation at Mn sites—successfully integrates O_3 activation and CH_3SH degradation into a self-accelerating ozonation process.

2 | Results and Discussion

2.1 | Structural Characterization and Catalytic Performance of $Cu_xMn_{3-x}O_4$ Catalysts

To elucidate the structure–activity relationship of the designed catalysts, we first conducted systematic structural and catalytic performance characterization. As shown in Figure 1a, the X-ray diffraction (XRD) pattern of the pristine Mn_3O_4 is consistent with tetragonal hausmannite (JCPDS No. 24-0734) [25]. This tetragonal distortion from the ideal cubic spinel structure is a classic manifestation of the Jahn–Teller effect associated with octahedrally coordinated Mn^{3+} ions ($t_{2g}^3 e_g^1$). Notably, a structural evolution from tetragonal to cubic symmetry is observed with increasing Cu content, which aligns well with the cubic spinel structure (JCPDS No. 74-2422) [25]. This transition indicates that Cu doping effectively suppresses the Jahn–Teller distortion, implying a more symmetric electronic environment around the Mn ions that facilitates electron delocalization. Raman and Fourier-Transform Infrared Spectroscopy (FTIR) further confirm the structural evolution. The Raman spectra (Figure S1a) show a systematic blueshift of the A_{1g} mode (~650 cm^{-1}) with increasing Cu content, indicating strengthened Mn—O bonds due to Jahn–Teller distortion suppression—consistent with cubic phase stabilization in XRD [28, 29]. Correspondingly, the evolution of M—O vibration bands in FTIR (Figure S1b) verifies the modified of the local coordination environment, confirming the successful formation of the Cu—Mn spinel solid solution [30]. As illustrated in Figure 1b, Cu occupies tetrahedral A sites and couples with octahedral Mn via A—O—B bridges, establishing a scaffold for cross-site charge transport.

Scanning electron microscopy (SEM) reveals all samples consist of micron-scale aggregates assembled from nanosized subunits, with Cu incorporation introducing no secondary phases or drastic morphological changes (Figure S2) [31]. High-resolution transmission electron microscopy (HRTEM) images show pristine Mn_3O_4 (Figure S3) exhibits clear lattice fringes of 0.28 and 0.31 nm, corresponding to the (103) and (112) planes of tetragonal Mn_3O_4, respectively. In contrast, the optimal $Cu_{0.75}Mn_{2.25}O_4$ catalyst (Figure S4) displays interplanar spacings of 0.49 and 0.23 nm, indexed to the (101) and (311) planes of the cubic spinel structure [32, 33]. Moreover, energy-dispersive X-ray spectroscopy (EDS) mapping (Figures S3 and S4) demonstrates the homogeneous

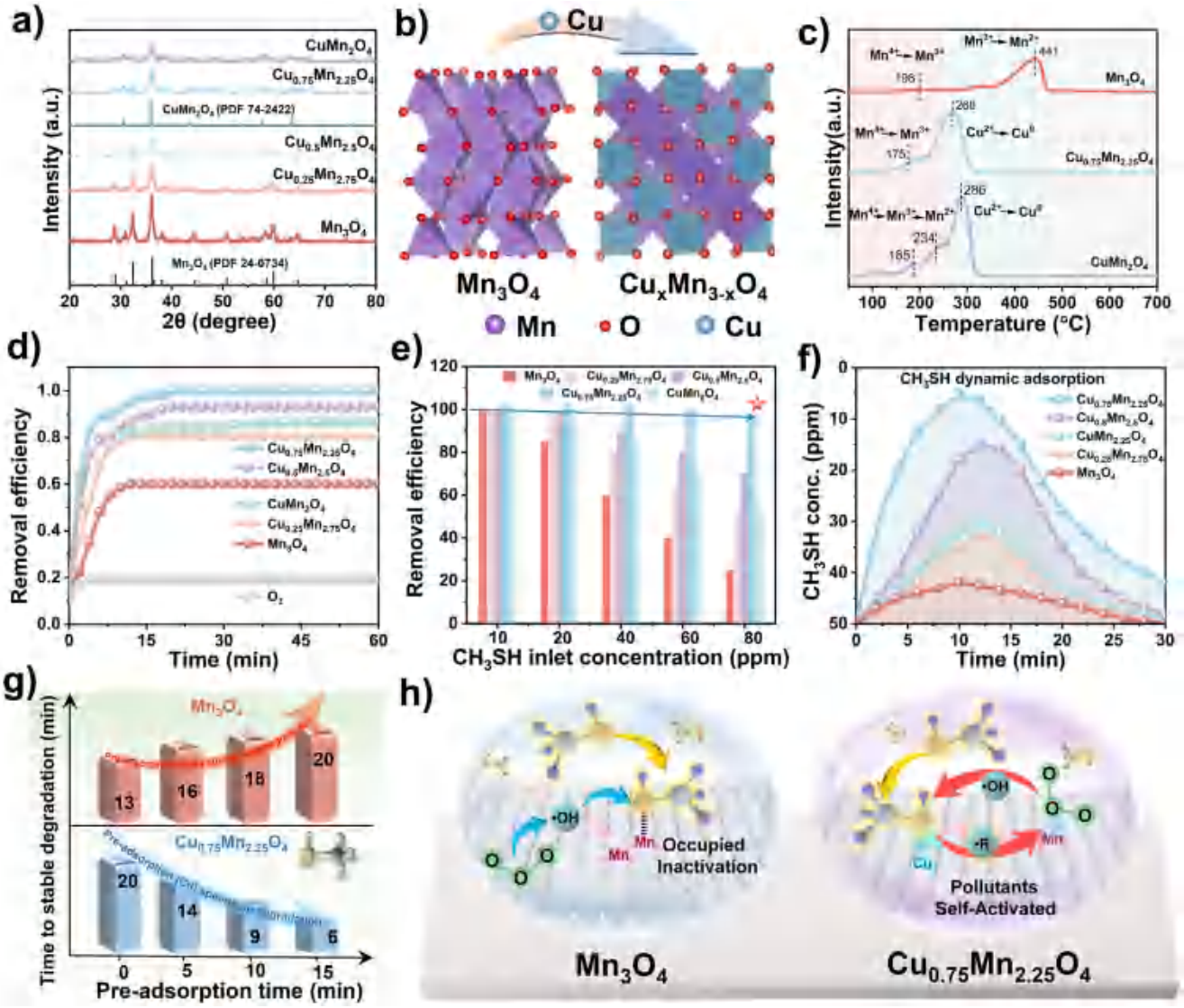

FIGURE 1 | a) XRD patterns of $Cu_xMn_{3-x}O_4$. b) Schematic illustration of spinel structure modification. c) H_2-TPR profiles of Mn_3O_4, $Cu_{0.75}Mn_{2.25}O_4$, and $CuMn_2O_4$. d) Catalytic ozonation performance for CH_3SH degradation over different catalysts (CH_3SH: 50 ppm, O_3: 35 ppm, total flow rate: 100 mL min^{-1}). e) CH_3SH removal efficiency over various catalysts at different inlet CH_3SH concentrations. f) Dynamic adsorption curves of CH_3SH on different catalysts. g) Effect of CH_3SH pre-adsorption time on the time required to reach stable degradation. h) Schematic illustration of proposed reaction processes.

distribution of Cu, Mn, and O elements throughout the particles, confirming the formation of a homogeneous Cu-Mn-O solid solution without phase segregation. The elemental compositions determined by ICP-OES are listed in Table S1. N_2 physisorption (Figure S5) shows all samples have comparable BET surface areas and pore size distributions, indicating the dramatic catalytic activity enhancement stems from intrinsic chemical properties modulated by Cu doping rather than physical textural differences.

The redox behavior of the catalysts—critical for O_3 activation efficiency, was investigated by H_2-temperature programmed reduction (TPR) (Figure 1c). The Mn_3O_4 profile shows two characteristic reduction peaks at approximately 198 and 441°C, corresponding to the sequential reduction of Mn^{4+} to Mn^{3+} and Mn^{3+} to Mn^{2+}, respectively [34, 35]. With Cu incorporation, a new reduction peak emerges at 270–290°C (attributed to the reduction of Cu^{2+} to Cu^0), while Mn-related reduction shifts to lower temperatures—indicating hydrogen spillover and strong Cu—Mn redox coupling via A—O—B bridges. The $Cu_{0.75}Mn_{2.25}O_4$ catalyst exhibits the most intense low- and mid-temperature peaks, reflecting the highest redox mobility and the most labile lattice oxygen. The pronounced shift of the reduction events to lower temperatures clearly demonstrates that Cu doping markedly enhances reducibility and creates highly active sites for electron transfer.

X-ray photoelectron spectroscopy (XPS) was used to decipher surface chemical states (Figure S6). Cu 2p XPS shows main peaks of Cu^{2+} with shake-up satellites, accompanied by a discernible Cu^+ component; the $Cu^+/(Cu^+ + Cu^{2+})$ fraction increases upon Cu addition and reaches a maximum at $x \approx 0.75$, then slightly declines at $x = 1.0$. Mn 2p spectra show a gradual shift toward higher effective oxidation state (enhanced Mn^{4+}, suppressed Mn^{2+}/Mn^{3+}) upon Cu doping, again peaking near $x \approx 0.75$. O 1s

deconvolution reveals Cu introduction increases the proportion of surface oxygen species (O_v/O_{ads}) relative to lattice oxygen (O_{latt}) [36]. This optimized surface configuration—balanced Cu^+/Cu^{2+} pair, prevalent Mn^{4+}/Mn^{3+} couple, and abundant reactive oxygen species—creates an ideal electronic environment for efficient Cu—O—Mn spin channels, providing the essential surface redox platforms for the •H-triggered chain reaction.

Catalytic performances for CH_3SH degradation in Figure 1d. Under identical reaction conditions, pristine Mn_3O_4 exhibited limited activity (~60% removal). Cu incorporation markedly enhances performance, with activity following the order: Mn_3O_4 < $Cu_{0.25}Mn_{2.75}O_4$ < $Cu_{0.5}Mn_{2.5}O_4$ < $CuMn_2O_4$ < $Cu_{0.75}Mn_{2.25}O_4$. Impressively, the optimal $Cu_{0.75}Mn_{2.25}O_4$ catalyst achieved complete CH_3SH removal with exceptional stability, underscoring the critical role of the optimized Cu/Mn ratio. The sustained, complete removal under continuous flow cannot be explained by adsorption saturation but points to an efficient and regenerative catalytic cycle. Electron paramagnetic resonance (EPR) signals at $g \approx 2.003$ (Figure S7, associated with O_v) show no positive correlation with activity—the most intense O_v signal is observed for the suboptimal $Cu_{0.5}Mn_{2.5}O_4$, while the best-performing $Cu_{0.75}Mn_{2.25}O_4$ exhibits a moderate signal—demonstrating oxygen vacancies are not the primary driver. Furthermore, control experiments with Zn-doped spinels ($Zn_xMn_{3-x}O_4$, Figures S8–S10) confirm enhanced activity is unique to Cu doping. Unlike redox-active Cu^{2+}, redox-inert Zn^{2+} (d^{10} configuration) fails to improve performance beyond Mn_3O_4, indicating the exceptional activity of $Cu_xMn_{3-x}O_4$ originates from specific redox activity and electronic synergy of Cu species in the spinel structure.

As shown in Figure S11, adding TBA severely suppresses CH_3SH removal in both the Mn_3O_4/O_3 and $Cu_{0.75}Mn_{2.25}O_4/O_3$ systems, confirming •OH as the dominant oxidant. Catalysts were further tested under varying inlet CH_3SH concentrations (Figure 1e). For Mn_3O_4, removal efficiency drops sharply from 75% to 25% as concentration increases from 20 to 80 ppm, indicative of active-site saturation and severe poisoning by the pollutant or its intermediates. In stark contrast, $Cu_{0.75}Mn_{2.25}O_4$ maintains high performance (100% to 92% over the same range), demonstrating remarkable tolerance to high pollutant loads and superior anti-poisoning capability. This stability under high pollutant flux further rules out the possibility that the high removal efficiency in Figure 1d is primarily due to physisorption as an adsorption-dominated process would show rapid efficiency decay with increasing concentration, as seen for Mn_3O_4. This superior stability is attributed to a unique interaction between CH_3SH and the Cu sites in $Cu_{0.75}Mn_{2.25}O_4$, where adsorbed CH_3SH is not merely a passivating species but is activated to initiate a surface-mediated process that facilitates continuous active sites regeneration. Collectively, these results confirm that the superior performance of $Cu_{0.75}Mn_{2.25}O_4$ in Figure 1d stems from a catalytic ozonation process in which strong adsorption is a necessary and functional first step, enabling the •H-triggered chain reaction that leads to deep mineralization. Post-reaction XRD (Figure S12) confirms the spinel structure remains intact with no phase segregation or altered crystallinity. XPS (Figure S13) reveals surface chemical states of Cu and Mn nearly revert to initial states after reaction, indicating a dynamic, reversible redox cycle crucial for long-term stability and sulfur poisoning resistance.

Combined adsorption and pre-adsorption experiments elucidate distinct catalyst behaviors under CH_3SH exposure (Figure 1f,g). $Cu_{0.75}Mn_{2.25}O_4$ exhibits a markedly higher CH_3SH adsorption capacity than Mn_3O_4. More importantly, the effect of this adsorption on subsequent catalytic ozonation is fundamentally different: increasing pre-adsorption time progressively slows the degradation kinetics over Mn_3O_4 (classical site blocking), while the opposite trend is observed for $Cu_{0.75}Mn_{2.25}O_4$ (longer pre-adsorption shortens time to stable degradation). This counterintuitive synergy strongly suggests adsorbed CH_3SH is actively involved in a surface-mediated process. We thus propose a synergistic catalytic model (Figure 1h): on Mn_3O_4, CH_3SH, and O_3 compete for the same sites, leading to catalyst poisoning; on $Cu_{0.75}Mn_{2.25}O_4$, Cu sites preferentially adsorb and activate CH_3SH, while Mn sites selectively activate O_3. This division of labor avoids competitive adsorption and establishes an efficient electron-transfer pathway, enabling "self-activated" pollutant degradation and sustained catalytic regeneration.

2.2 | Mechanistic Investigation of the Catalytic Ozonation Process

To unravel the distinct reaction pathways of CH_3SH catalytic ozonation over different catalysts, we conducted in situ diffuse reflectance infrared Fourier-transform spectroscopy (DRIFTS), product analysis, and element balance studies. In situ DRIFTS of CH_3SH adsorption (Figure 2a,d) reveals distinct interaction modes on Mn_3O_4 and $Cu_{0.75}Mn_{2.25}O_4$. For $Cu_{0.75}Mn_{2.25}O_4$, the ν(C—H) stretching vibration of CH_3S^- (2960–2850 cm^{-1}) is significantly stronger than on Mn_3O_4, indicating enhanced adsorption of CH_3S^- species [37]. This stems from strong coordination between Cu^{2+} (empty 3d orbitals) and S atoms (lone-pairs donors), forming stable Cu—S bonds. Conversely, the ν(S—H) band (2570 cm^{-1}) is weaker on $Cu_{0.75}Mn_{2.25}O_4$ and diminishes over time, while Mn_3O_4 shows persistent, stronger ν(S—H) signals. This suggests that Cu doping promotes S—H bond homolysis during adsorption to generate surface-bound CH_3S^- species, whereas Mn_3O_4 primarily adsorbs intact CH_3SH via hydrogen bonding with minimal S—H cleavage (Figure 2g). Notably, weak but distinct peaks emerge in both spectra, indicative of mild oxidation CH_3SH by surface-adsorbed oxygen species-including CH_3OH (1048 cm^{-1}, C—O stretching), SO_3^{2-} (848 cm^{-1}), SO_2 (754 cm^{-1}), and trace SO_4^{2-} (1181 cm^{-1}) [8, 9, 38]. These peaks are slightly more intense on $Cu_{0.75}Mn_{2.25}O_4$, confirming Cu doping enhances the reactivity of surface oxygen species.

During catalytic ozonation (Figure 2b,e), the $\nu(CH_3S^-)$ band on $Cu_{0.75}Mn_{2.25}O_4$ gradually diminishes, accompanied by transient peaks at 1150 cm^{-1} (CH_3SSCH_3, disulfide) and 1030 cm^{-1} (SO_3^{2-})—which rise within 10 min and then decline. Concurrently, the $\nu(SO_4^{2-})$ band (1100–1080 cm^{-1}) strengthens continuously, indicating stepwise oxidation of CH_3S^- to sulfate. In contrast, Mn_3O_4 retains intense $\nu(CH_3S^-)$ signals throughout the reaction, with weak and persistent SO_3^{2-} peaks and negligible SO_4^{2-} formation-signaling severe accumulation of methylthiolate intermediates and sluggish mineralization. The near disappearance of ν(S—H) on $Cu_{0.75}Mn_{2.25}O_4$ during ozonation further confirms that pre-activated CH_3S^- species are readily oxidized, whereas unbroken S—H bonds on Mn_3O_4 hinder subsequent reactions.

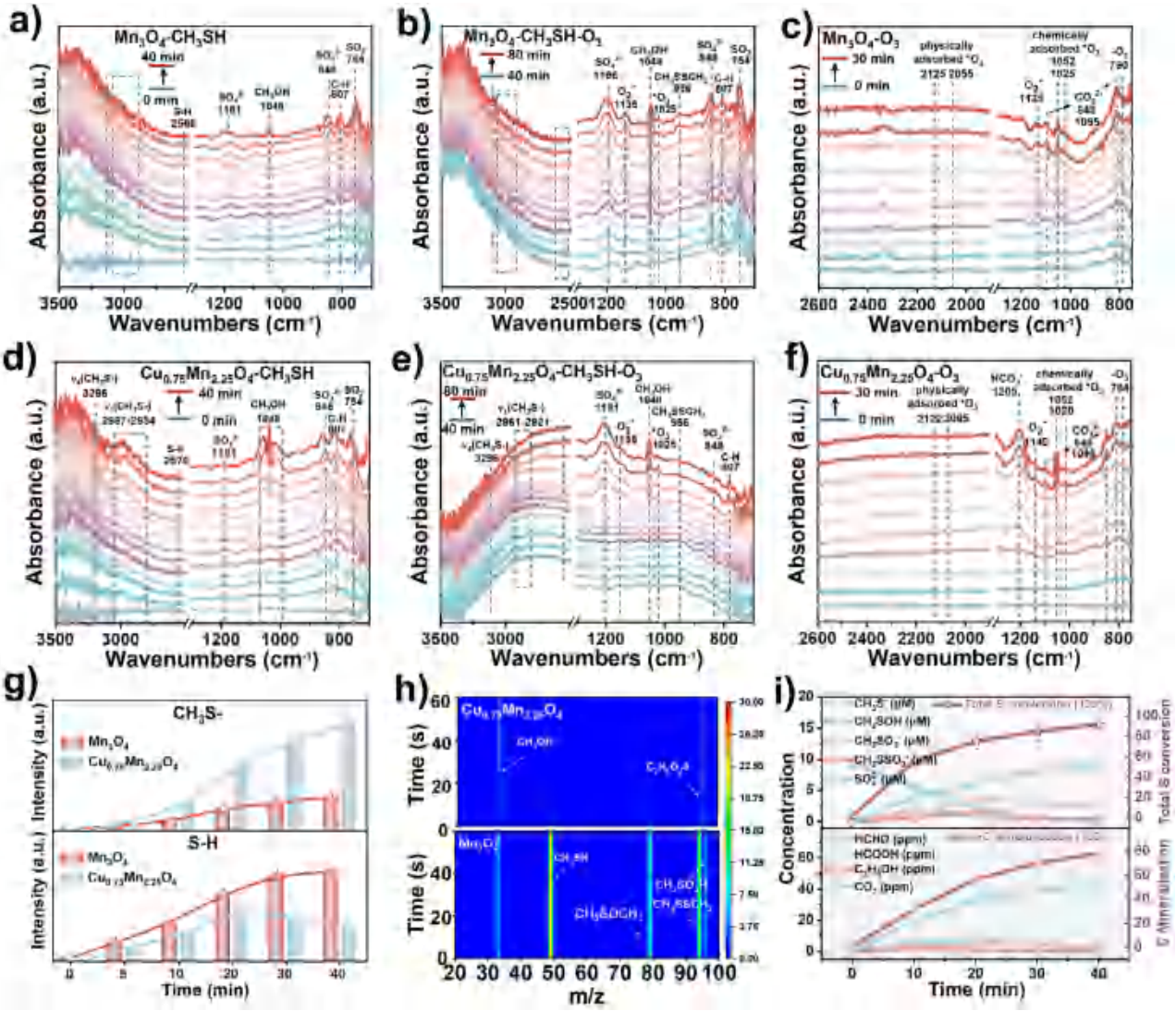

FIGURE 2 | In situ DRIFTS spectra of Mn_3O_4 for (a) CH_3SH adsorption (0–40 min), b) subsequent catalytic ozonation (40–80 min), and c) O_3 adsorption (0–30 min). Corresponding in situ DRIFTS spectra of $Cu_{0.75}Mn_{2.25}O_4$ under the same conditions: d) CH_3SH adsorption, e) catalytic ozonation, and f) O_3 adsorption. g) Temporal evolution of the relative intensities of the CH_3S^- and S—H vibrational bands during CH_3SH adsorption on Mn_3O_4 and $Cu_{0.75}Mn_{2.25}O_4$. h) PTR-TOF-MS analysis of outlet gases after 40 min of catalytic ozonation over $Cu_{0.75}Mn_{2.25}O_4$ and Mn_3O_4. i) Time-dependent concentration profiles of key sulfur/carbon species and the total conversion/mineralization efficiency in the $Cu_{0.75}Mn_{2.25}O_4/O_3/CH_3SH$ system.

In situ DRIFTS of O_3 adsorption (Figure 2c,f) highlights differences in O_3 activation. $Cu_{0.75}Mn_{2.25}O_4$ exhibits stronger bands at 1052 and 1020 cm^{-1}, assigned to chemisorbed $*O_3$ and surface-bound atomic oxygen (*O), indicating efficient O_3 activation. Notably, a peak at 1360 cm^{-1} (HCO_3^-) emerges on $Cu_{0.75}Mn_{2.25}O_4$ but not on Mn_3O_4, suggesting concurrent oxidation of carbon-containing intermediates to carbonate species [21]. Proton-transfer-reaction time-of-flight mass spectrometry (PTR-TOF-MS) of outlet gases (Figure 2h) confirms these mechanistic differences: $Cu_{0.75}Mn_{2.25}O_4$ produces primarily CO_2 and H_2O, with negligible residual CH_3SH or intermediates (e.g., CH_3OH, CH_3SSCH_3), while Mn_3O_4 emits unreacted CH_3SH and various partial oxidation products. Element balance analysis (Figure 2i) quantifies this: $Cu_{0.75}Mn_{2.25}O_4$ achieves >95% S conversion (to SO_4^{2-}) and >90% C conversion (to CO_2) within 40 min, with transient intermediates (e.g., CH_3S^-, SO_3^{2-}) remaining at low concentrations. In contrast, Mn_3O_4 shows <40% S/C conversion, with persistent accumulation of methylthiolates and organic sulfides. Collectively, these results demonstrate Cu doping modulates two key steps: (1) promoting CH_3SH adsorption via Cu—S coordination and S—H bond activation; (2) enhancing O_3 chemisorption and activation to drive efficient oxidation of intermediates to mineralized products. This dual role underpins the superior performance of $Cu_{0.75}Mn_{2.25}O_4$ over Mn_3O_4.

2.3 | •H-Triggered Chain Reaction and Spinel Spin Channels

Having established the distinct reaction pathways, we aimed to identify the key active species and elucidate the underlying electronic mechanism. Electron paramagnetic resonance (ESR) spectroscopy directly confirmed radical generation (Figure 3a), Characteristic signals of both DMPO-•H and

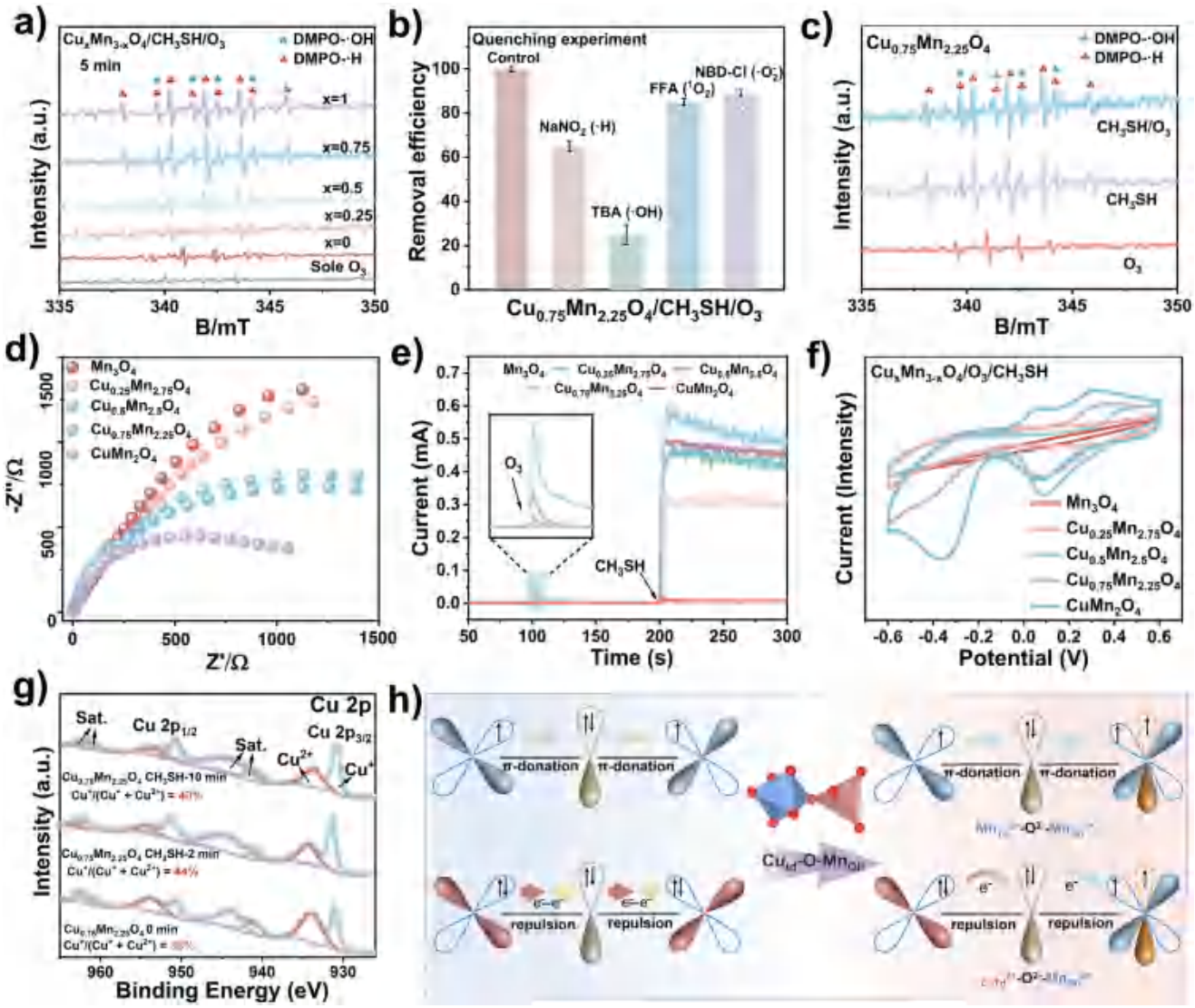

FIGURE 3 | a) DMPO-•H and DMPO-•OH adducts in $Cu_xMn_{3-x}O_4/CH_3SH/O_3$ systems. b) CH_3SH removal efficiency in quenching experiments over $Cu_{0.75}Mn_{2.25}O_4$. c) DMPO-•H and DMPO-•OH adducts over $Cu_{0.75}Mn_{2.25}O_4$ under CH_3SH/O_3, CH_3SH, and O_3 conditions. d) Electrochemical impedance spectroscopy (EIS) Nyquist plots of different $Cu_xMn_{3-x}O_4$ catalysts. e) I–t curves of $Cu_xMn_{3-x}O_4$ catalysts upon sequential introduction of O_3 and CH_3SH. f) Cyclic voltammetry (CV) curves of different $Cu_xMn_{3-x}O_4$/ catalysts. g) Cu 2p for $Cu_{0.75}Mn_{2.25}O_4$ before and after CH_3SH adsorption. h) Schematic of O 2p-transition metal 3d electronic interactions.

DMPO-•OH adducts were simultaneously detected in the $Cu_xMn_{3-x}O_4/CH_3SH/O_3$ systems after 5 min, while no signals were observed in the sole O_3 system [39–43]. The intensity of both radical signals strongly correlated with Cu content, peaking at x = 0.75. Notably, pristine Mn_3O_4 generated a weak •OH signal, underscoring the indispensable role of Cu in triggering •H formation. Complementary ESR results (Figure S14) reveal Cu doping also enhances $^1O_2$ signal intensity, while $\cdot O_2^-$ signals remain negligible across all systems. Quenching experiments quantified the contributions of these radicals (Figure 3b). Adding *tert*-butanol (TBA, •OH quencher) severely suppressed CH_3SH degradation, confirming •OH as the primary reactive oxygen species. Strikingly, the introduction of $NaNO_3$ (•H quencher) also caused a dramatic activity drop [39]. This result not only verifies the non-negligible role of •H but also suggests interconversion between •H and •OH-wherein •H serve as a precursor for massive •OH generation.

To validate this hypothesis, we examined radical evolution over $Cu_{0.75}Mn_{2.25}O_4$ under different conditions (Figure 3c). In the sole CH_3SH stream, the DMPO-•H signal was observed, unequivocally identifying Cu sites as the active centers for S—H bond homolysis. With only O_3 present, solely the DMPO-•OH signal was detected. Critically, when both CH_3SH and O_3 were introduced, the •OH signal intensified markedly while the •H signal concurrently weakened. This complementary dynamic provides strong evidence that the •H generated from CH_3SH dissociation is rapidly consumed to promote O_3 activation into •OH, thus initiating a productive chain reaction.

The superior activity of Cu-doped catalystsoriginates from enhanced electronic conductivity, probed by electrochemical impedance spectroscopy (EIS) and current–time (i–t) measurements. $Cu_{0.75}Mn_{2.25}O_4$ exhibits the smallest arc radius in EIS Nyquist plots (Figure 3d) and the highest current response upon

O_3 and CH_3SH introduction (Figure 3e), indicating the most efficient charge transfer and the fastest surface reaction kinetics. Cyclic voltammetry (CV) (Figure 3f) and linear sweep voltammetry (LSV, Figure S15) further corroborate this: $Cu_{0.75}Mn_{2.25}O_4$ shows the highest redox current density and lowest onset potential, signifying optimal electron acceptance and delivery capabilities.

To trace the electron flow at the atomic level, in situ XPS was conducted. After a 2-min exposure to CH_3SH, the $Cu^+/(Cu^+ + Cu^{2+})$ ratio on $Cu_{0.75}Mn_{2.25}O_4$ increased substantially from 30% to 44% (Figure 3g), confirming electron donation from CH_3SH to Cu sites. When the interaction prolonged to 10 min, the Cu^+ ratio slightly decreased to 40%, while the Mn 2p spectrum (Figure S16) showed a noticeable increase in lower-valence Mn species. This electron transfer sequence—from CH_3SH to Cu and subsequently to Mn—visually captures the electron relay along the Cu—O—Mn spin channel.

The electronic structure basis for this efficient channel is depicted in Figure 3h. Cu^{2+} ($3d^9$) introduces strong electron repulsion with the O 2p orbitals, elevating the energy level and spin density of the lattice oxygen. This activated oxygen bridge facilitates π-donation to the Mn^{3+} ($3d^4$) center, promoting electron delocalization across the metal-oxygen-metal framework. This unique interaction establishes a low-energy pathway for electron transfer, meeting the continuous electron demand for O_3 activation and enabling the sustained •H-triggered chain reaction.

2.4 | Electronic Structure and Spin-State Modulation

To elucidate the origin of the superior catalytic activity and the unique •H-triggered reaction pathway, we systematically probed the electronic structure and spin configuration of the $Cu_xMn_{3-x}O_4$ catalysts. Combining synchrotron-based X-ray absorption spectroscopy (XAS), magnetic measurements, and density functional theory (DFT) calculations, we show that Cu doping effectively tailors the local coordination, density of states, and spin-polarized electron transport, culminating in the establishment of highly efficient spin channels essential for catalytic ozonation. Mn K-edge X-ray absorption near-edge structure (XANES) spectra (Figure 4a) show the absorption edge of $Cu_{0.75}Mn_{2.25}O_4$ lies between Mn_3O_4 and MnO_2, indicating an elevated average Mn oxidation state upon Cu incorporation, consistent with XPS results. Fourier-transformed EXAFS (Figure 4b) reveals $Cu_{0.75}Mn_{2.25}O_4$ retains a first-shell Mn—O peak similar to Mn_3O_4, while the second-shell feature shifts to lower R with reduced intensity. This suggests increased structural disorder and the presence of lighter backscatterers. This second-shell configuration is consistent with mixed Mn—O—Mn/Cu scattering paths, confirming Cu incorporation into the Mn lattice without phase segregation. Wavelet transform (WT) analysis provides further spatial resolution: the Mn K-edge WT plot of $Cu_{0.75}Mn_{2.25}O_4$ (Figure 4c, top row) exhibits an intensified and broadened intensity maximum in the Mn-M region (where "M" denotes all neighboring metal atoms, i.e., Mn and Cu in the doped spinel) compared to the sharper Mn—Mn contribution in Mn_3O_4 (where "M" exclusively refers to Mn). The broadening and shift of this feature directly signal the replacement of some Mn neighbors with lighter Cu atoms, forming mixed Mn-Mn (homometallic) and Mn-Cu (heterometallic) scattering paths. Complementary analysis at the Cu K-edge (XANES: Figure S18a–c; EXAFS and WT: Figure 4c bottom row and Figure S18d–h) confirms the local environment of the dopant. The Cu K-edge XANES shows an absorption edge near CuO (slightly lowered), consistent with predominantly Cu^{2+} with a minor Cu^+ fraction. The corresponding WT plot (Figure 4c, bottom row) displays a clear Cu-M feature (where "M" denotes neighboring Mn atoms) originating from Cu—Mn backscattering, without detectable Cu—Cu signals. This, together with EXAFS results showing a prominent Cu—O first shell and a second shell aligned with Cu—Mn distance, confirms the atomic-level incorporation of Cu into the spinel lattice and the formation of oxygen-bridged Cu—O—Mn linkages—the structural basis for cross-site electronic communication.

Magnetic susceptibility measurements (M—T curves) reveal a paramagnetic behavior for all samples at high-temperature regime. Curie–Weiss plots (Figure 4d) show $Cu_{0.75}Mn_{2.25}O_4$ has the largest slope, smallest Curie constant, and lowest effective moment (μ_{eff} = 2.04 μB, Figure 4e). DFT reproduces this trend: the calculated local moment of Mn^{3+} decreases upon Cu substitution and reaches a minimum at $x \approx 0.75$ (Figure S19; Tables S2–S4), Spin-density maps (Figure S19d–f) show increased electron delocalization toward the anion framework. Oxygen-magnetization statistics (Figure 4f) confirm appreciable O-2p polarization for all samples, with redistribution of O-site moments upon Cu doping; the inset O-2p PDOS exhibits greater spectral weight near the Fermi level (E_f) and discernible spin asymmetry for $Cu_{0.75}Mn_{2.25}O_4$—indicating stronger p–d participation of lattice oxygen in the exchange network. Together, experiment and theory demonstrate Cu-induced reduction of local Mn moments and concurrent engagement of O-2p states, an electronic reorganization compatible with Cu—O—Mn spin-mediated interactions.

DFT calculations further clarify the structural origin of this optimized electronic configuration via Mn—O bond lengths and orbital-projected PDOS near E_f (Figures 4h and S20). $Cu_{0.75}Mn_{2.25}O_4$ exhibits the shortest Mn—O bond among the series (Table S5)—an contraction signifying a transition to a more symmetric, covalent bonding framework. This structural tightening, induced by Cu doping, directly reflects suppressed Jahn–Teller distortion, which dramatically strengthens overlap between O 2p and Mn 3d (e_g) orbitals. This intensified hybridization is evidenced by the most prominent PDOS peak near E_f, confirming the formation of a highly delocalized electron network essential for efficient Cu—O—Mn spin channels. This strengthened hybridization is further quantified by crystal orbital Hamilton population (COHP) analysis (Figure S21), which shows an integrated —ICOHP value of 1.61 eV for the octahedral Mn—O bond in $Cu_{0.75}Mn_{2.25}O_4$, significantly higher than the 0.65 eV in pristine Mn_3O_4. Concurrently, the tetrahedral Cu—O bond exhibits a —ICOHP of 1.76 eV, which is stronger than the 1.36 eV in over-doped $CuMnO_2$. Analysis of the COHP curves reveals that this increase arises from enhanced bonding interactions and reduced anti-bonding occupation, confirming the strongest metal–oxygen covalency and orbital overlap in the optimal catalyst. Consistently, electron localization function (ELF) (Figure S22) shows $Cu_{0.75}Mn_{2.25}O_4$ has a more delocalized electron distribution along M—O—M chains than Mn_3O_4, with weakened

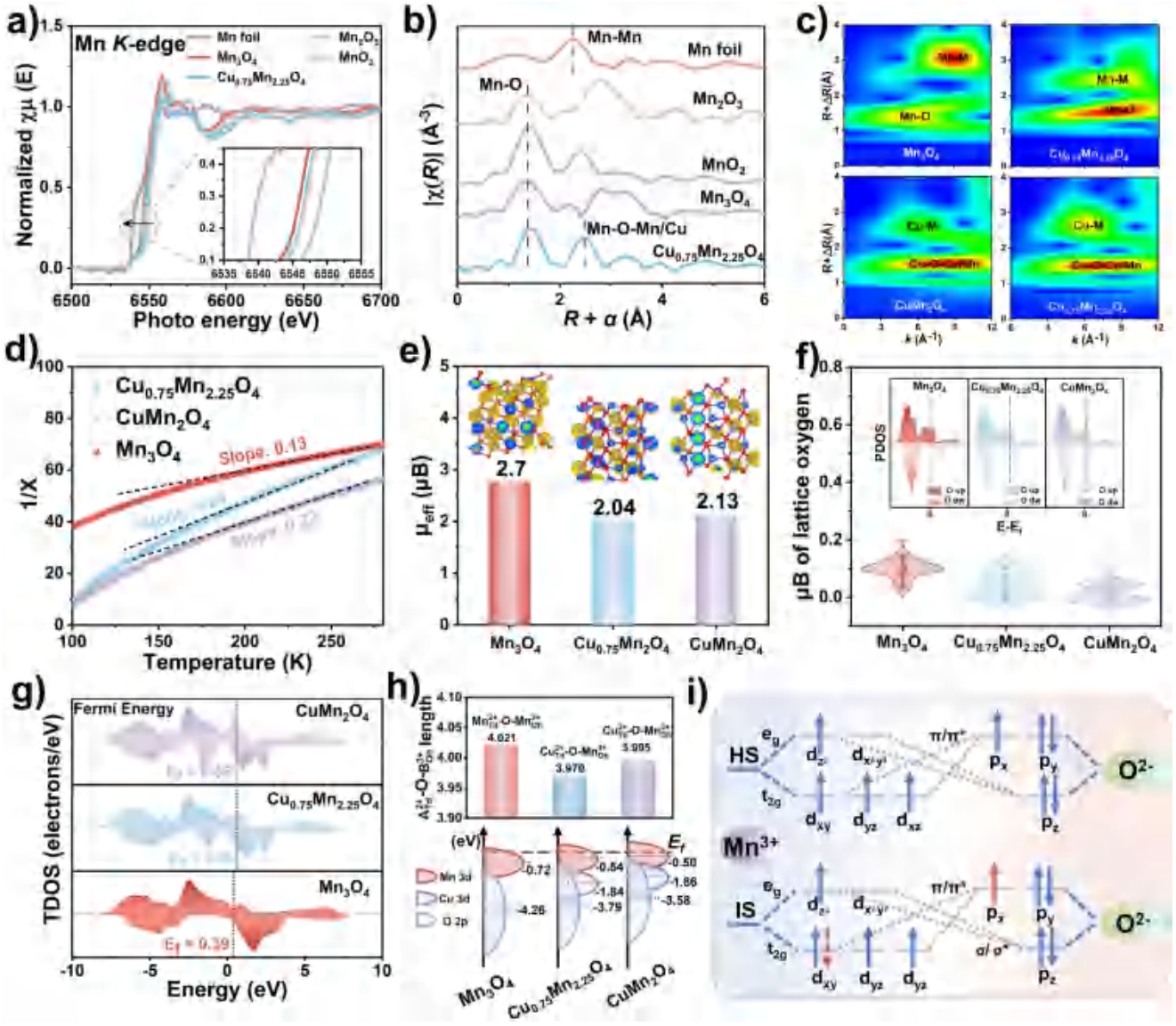

FIGURE 4 | a) Mn K-edge normalized XANES spectra of Mn foil, Mn_2O_3, MnO_2, Mn_3O_4, and $Cu_{0.75}Mn_{2.25}O_4$. b) Fourier-transformed EXAFS spectra ($|\chi(R)|$). c) Wavelet transform (WT) contour plots of (top row) Mn K-edge and (bottom row) Cu K-edge for the corresponding samples. The label "Mn-M (Mn/Mn-Cu)" denotes the scattering from photoabsorbing Mn to neighboring metal atoms (Mn for Mn_3O_4, Mn/Cu for $Cu_{0.75}Mn_{2.25}O_4$); "Cu-M (Cu-Mn)" denotes the exclusive scattering from photoabsorbing Cu to neighboring Mn atoms (no Cu-Cu scattering detected). d) Temperature-dependent inverse susceptibilities of $Cu_xMn_{3-x}O_4$. e) Calculated effective magnetic moments (μ_{eff}) of $Cu_xMn_{3-x}O_4$. f) The calculated bulk oxygen magnetization (μB) and partial density of states (PDOS) of lattice oxygen. g) Total density of states (TDOS) of Mn_3O_4, $Cu_{0.75}Mn_{2.25}O_4$, and $CuMn_2O_4$, with Fermi energy (E_f) marked. h) Calculated Mn-O bond lengths and orbital-resolved PDOS near the Fermi level for Mn_3O_4, $Cu_{0.75}Mn_{2.25}O_4$, and $CuMn_2O_4$. i) Schematic illustration of orbital interactions and spin configurations of Mn^{3+} (high-spin, HS; intermediate-spin, IS) with O^{2-} orbitals.

localization around individual Mn centers—corroborating that Cu doping suppresses Jahn–Teller-driven charge localization and promotes continuous Cu—O—Mn spin-conduction pathways.

This synergistic structural and electronic evolution is schematically summarized in Figure 4i, illustrating the underlying spin-state regulation. In pristine Mn_3O_4, the high-spin (HS) state of octahedral Mn^{3+} drives strong Jahn–Teller distortion, leading to electron localization. In contrast, Cu incorporation stabilizes an intermediate-spin (IS)-like configuration in Mn^{3+}, which suppresses the Jahn–Teller distortion. This critical change selectively enhances the σ-type overlap between the half-filled Mn e_g orbitals and the O 2p orbitals, establishing a highly conductive, low-resistance pathway for spin-polarized electron transfer along the Cu—O—Mn bridge. This atomic-level engineering completes the physical picture of the efficient spin channels—fundamental to the •H-triggered chain reaction.

2.5 | Orbital–Spin–Coupled CH_3SH Activation and •OH Oxidation

To unravel the origin of the distinct catalytic behaviors, we performed spin-polarized DFT calculations to probe the adsorption configurations, electronic interactions, and reaction energetics. DFT-optimized structures and charge-density difference analysis

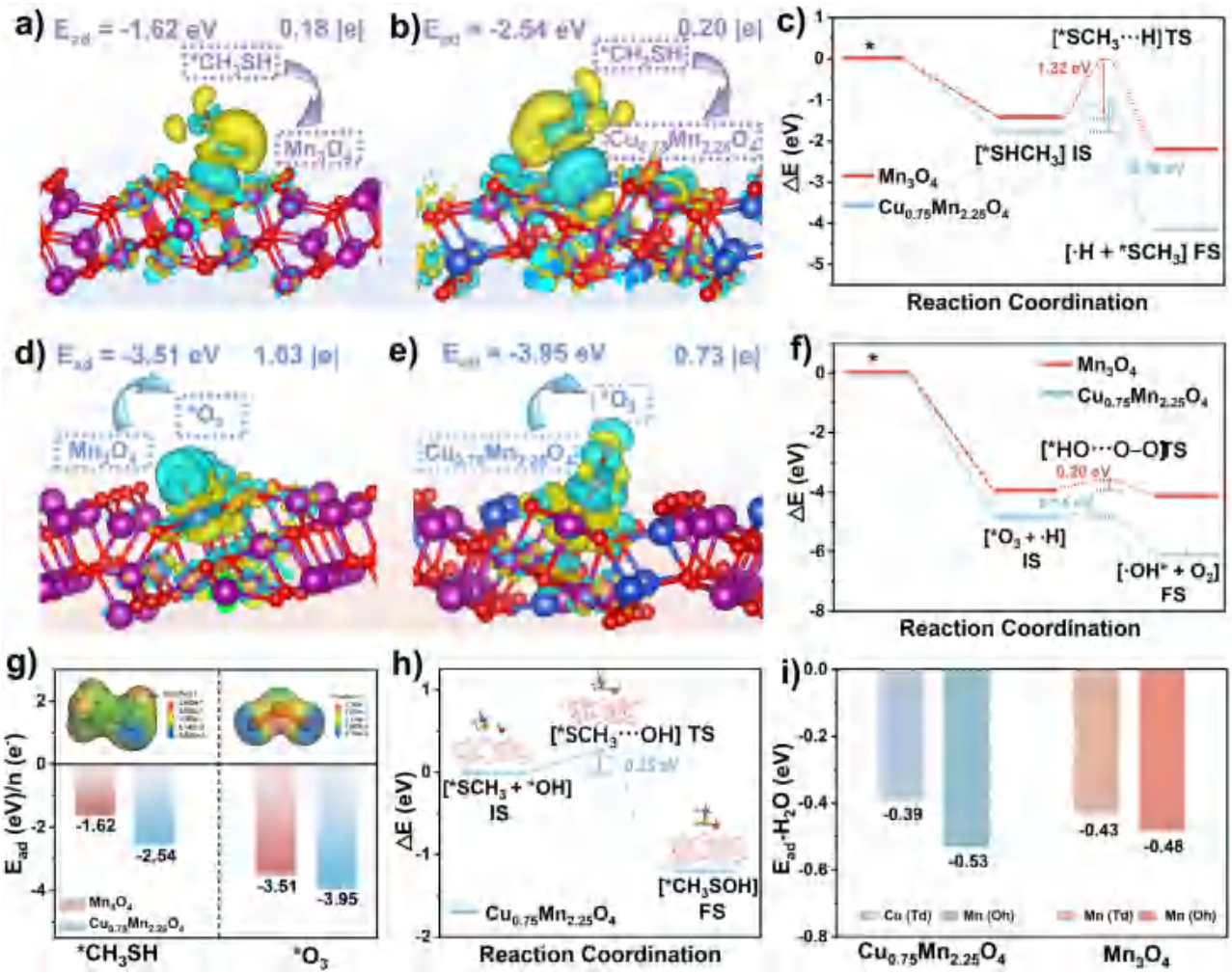

FIGURE 5 | Optimized configurations and charge-density difference isosurfaces for CH_3SH adsorption on a) Mn_3O_4 and b) $Cu_{0.75}Mn_{2.25}O_4$, with E_{ad} and Bader charge transfer (|e|) (isosurface value of 0.001 e Å^{-3}). c) Free-energy profiles for S—H homolysis of adsorbed CH_3SH on Mn_3O_4 and $Cu_{0.75}Mn_{2.25}O_4$. d) and e) Optimized structures and charge-density difference for O_3 adsorption, with E_{ad} and transferred charge indicated (isosurface value of 0.003 e Å^{-3}). f) Free-energy profiles for •H reacting with adsorbed O_3 on the two catalysts. g) Comparison of CH_3SH and O_3 adsorption energies. h) Free-energy diagram for the surface oxidation of $*SCH_3$ by *OH on $Cu_{0.75}Mn_{2.25}O_4$. i) H_2O adsorption energies on catalysts.

(Figure 5a,b) reveal fundamentally distinct modes on Mn_3O_4 and $Cu_{0.75}Mn_{2.25}O_4$. On Mn_3O_4, CH_3SH preferentially adsorbs on the Mn^{2+}(Td) site with an adsorption energy of −1.62 eV and a modest charge transfer of 0.18 |e|. In contrast, on $Cu_{0.75}Mn_{2.25}O_4$, CH_3SH binds much more strongly to Cu^{2+} (Td) (E_{ad} = −2.54 eV) with slightly larger electron donation (0.20 |e|), and the charge density difference map shows pronounced Cu—S coordination (Figure 5b). This robust adsorption directly facilitates S—H bond activation, as reflected in the free-energy profiles for S—H homolysis (Figure 5c). The free-energy barrier for splitting the adsorbed CH_3SH into •H and $*SCH_3$ reaches 1.32 eV on Mn_3O_4 but drops to 0.78 eV on $Cu_{0.75}Mn_{2.25}O_4$. This barrier reduction stems from stronger Cu—S covalency and enhanced electronic flexibility of the Cu-modified spinel, which jointly stabilize the radical-like transition state—consistent with the more intense DMPO—•H signals and faster •H production measured experimentally.

O_3 adsorption analysis (Figure 5d,e) shows O_3 binds more strongly to $Cu_{0.75}Mn_{2.25}O_4$ (E_{ad} = −3.95 eV) than to Mn_3O_4 (−3.51 eV), with greater electron transfer from the catalyst surface. This enhanced activation lowers the energy barrier for •H-induced O_3 reduction (Figure 5f). The free-energy profiles for •H attack on adsorbed O_3 indicate the rate-determining step—formation of the [*HO···O—O] transition state—has a barrier of 0.20 eV on Mn_3O_4, which further decreases to 0.14 eV on $Cu_{0.75}Mn_{2.25}O_4$. The overall process to generate surface •OH is strongly exergonic on both systems. These calculations confirm that once •H is supplied from the Cu site, its coupling with $*O_3$ at neighboring Mn sites is essentially barrierless at reaction temperature—enabling the experimentally observed "burst" generation of •OH and closing the •H-triggered O_3 activation loop. Comparative adsorption energies (Figure 5g) further highlight synergistic site specialization: Cu sites preferentially adsorb CH_3SH, while Mn sites favor O_3. This spatial separation of reactants naturally suppresses competitive adsorption and provides the geometric precondition for constructing Cu—O—Mn spin channels that relay •H and electrons between the two sites.

Subsequent oxidation of the surface-bound $*SCH_3$ species by •OH radicals proceeds via a low-barrier pathway on $Cu_{0.75}Mn_{2.25}O_4$,

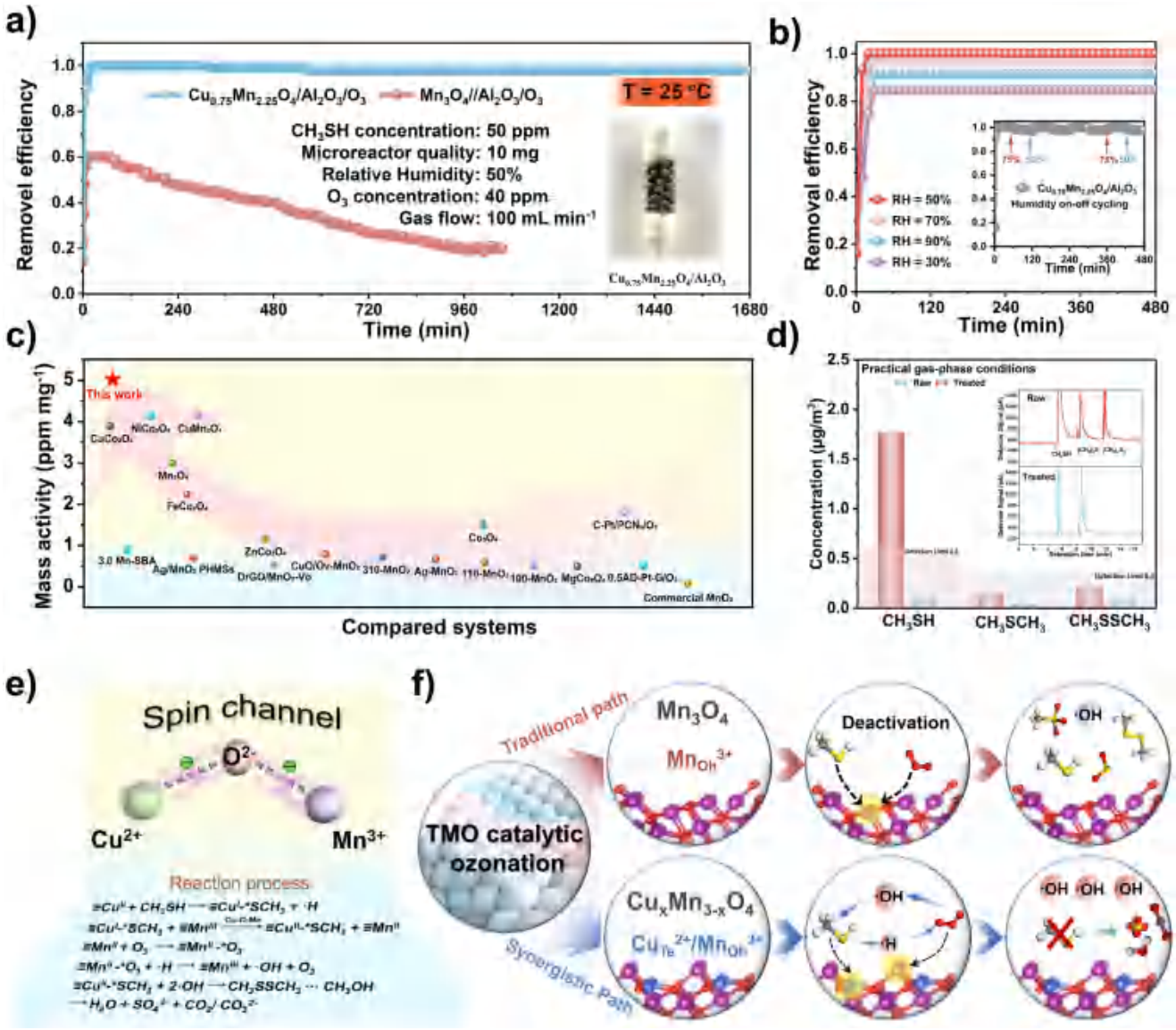

FIGURE 6 | a) CH_3SH removal efficiency over $Cu_{0.75}Mn_{2.25}O_4/Al_2O_3$ and Mn_3O_4/Al_2O_3. b) CH_3SH removal efficiency over $Cu_{0.75}Mn_{2.25}O_4/Al_2O_3$ under varied humidity and cycling tests. c) Mass activity comparison of $Cu_{0.75}Mn_{2.25}O_4$ with other CH_3SH oxidation catalytic systems. d) Catalytic performance under practical gas-phase conditions with real volatile malodorous organic compounds. e) Schematic of spin channel and CH_3SH catalytic ozonation reaction process. f) Mechanistic comparison between traditional TMO and synergistic $Cu_xMn_{3-x}O_4$ catalytic ozonation pathways.

ultimately yielding SO_4^{2-} and CO_2 (Figure 5h). The free-energy diagram shows the reaction between $*SCH_3$ and •OH to form $*CH_3SOH$ proceeds through a single transition state [$*SCH_3$•••OH] with a modest barrier of 0.25 eV. This indicates •OH-driven methylthiolate oxidation is both thermodynamically and kinetically facile—consistent with the rapid depletion of CH_3S^- and growth of sulfate observed in DRIFTS and ion-chromatography measurements. Once •H-assisted O_3 activation is triggered, subsequent •OH oxidation of $*SCH_3$ is no longer rate-limiting, ensuring efficient funneling of sulfur toward fully oxidized products. Water—ubiquitous in exhaust streams—modulates the reaction network as both a competitor and co-reactant. H_2O adsorption energies (Figure 5i) are moderate on both Cu (−0.39 eV) and Mn (−0.53 eV) sites in $Cu_{0.75}Mn_{2.25}O_4$—weaker than those of CH_3SH and O_3—preventing permanent site blocking while enabling beneficial hydration. The highest activity at RH ≈ 50% aligns with this balanced adsorption. As shown in Figure S23, surface *O reacts with H_2O via a [*O···HOH] transition state (barrier = 0.30 eV) to exergonically form *OH (ΔG = −0.70 eV), providing an auxiliary •OH source under humid conditions. In summary, DFT reveals a compact mechanism: Cu sites drive CH_3SH adsorption and S—H homolysis to •H; Mn sites activate O_3, which reacts barrierlessly with •H to yield •OH; •OH rapidly oxidizes $*SCH_3$ and intermediates; H_2O acts as a mild modulator rather than a poison. This orbital–spin–coupled hierarchy underpins the •H-triggered self-accelerating ozonation on $Cu_{0.75}Mn_{2.25}O_4$.

2.6 | Robust Catalytic Performance and Mechanistic Elucidation

To assess the practical applicability and durability of the catalyst, $Cu_{0.75}Mn_{2.25}O_4$ was loaded onto an Al_2O_3 support and tested

under continuous flow conditions (Figure S24). A controlled CH_3SH—O_3 gas mixture was continuously introduced into the fixed-bed microreactor, enabling real-time monitoring of CH_3SH removal. As shown in Figure 6a, the $Cu_{0.75}Mn_{2.25}O_4/Al_2O_3$ catalyst maintained nearly 100% CH_3SH conversion for over 28 h (1680 min), demonstrating remarkable long-term stability. In contrast, undoped Mn_3O_4/Al_2O_3 underwent rapid deactivation—confirming that Cu doping effectively enhances redox reversibility and oxygen mobility in the spinel lattice. The strong Cu—Mn synergistic interaction promotes continuous lattice oxygen regeneration and suppresses active-site poisoning, ensuring sustained catalytic oxidation under steady-state operation.

As illustrated in Figure 6b, $Cu_{0.75}Mn_{2.25}O_4/Al_2O_3$ retained high removal efficiency across different humidity conditions, with optimal performance at RH = 50%. Both lower (30%) and higher (90%) humidity caused slight activity declines, attributed to the humidity-dependent surface redox environment. At moderate humidity, an optimal density of surface hydroxyls forms, facilitating reactant adsorption and accelerating Cu^{2+}/Cu^{+} and Mn^{4+}/Mn^{3+} redox cycles. Insufficient humidity limits surface activation and oxygen mobility, while excessive humidity induces water over-adsorption—blocking active sites and hindering gas diffusion. Humidity on–off cycling further confirmed the catalyst's structural robustness and reversible surface chemistry, ensuring stable performance under fluctuating environmental conditions.

The superior activity of $Cu_{0.75}Mn_{2.25}O_4/Al_2O_3$ was highlighted by comparing its mass activity with reported CH_3SH oxidation systems (Figure 6c). It exhibits a mass activity approaching 5 ppm•mg^{-1}, markedly higher than most previously reported materials. Conventional single-metal oxides (e.g., Mn_3O_4, Co_3O_4, and $FeCo_2O_4$) show limited activity due to sluggish oxygen mobility and less efficient redox cycling. Bimetallic spinel catalysts (e.g., $NiCo_2O_4$, $CuMn_2O_4$, $CuCo_2O_4$) demonstrate moderate enhancement but fail to maintain long-term stability. Supported/modified systems (e.g., Ag/MnO_2, $Cu/Ov\text{-}MnO_2$, Pt–graphene, C—Pt/PCN) often rely on expensive or unstable active sites, limiting large-scale application [7, 10, 26, 27, 38, 44–47]. In contrast, $Cu_{0.75}Mn_{2.25}O_4$ integrates strong Cu—Mn redox synergy with spinel structural stability, achieving both high intrinsic activity and excellent durability—underlining its potential as a cost-effective, scalable alternative to noble-metal catalysts for practical CH_3SH abatement. To further validate practical applicability, the $Cu_{0.75}Mn_{2.25}O_4/Al_2O_3$ catalyst was evaluated with real petrochemical volatile malodorous organic compounds (VMOs). Gas chromatography analysis (Figures 6d and S25a–d) and concentration quantification (Tables S6 and S7) confirmed that the three key sulfur-containing pollutants (methanethiol, dimethyl sulfide, dimethyl disulfide) in the treated effluents were all below their respective method detection limits in two parallel tests, verifying the catalyst's reliable purification performance in complex real gas matrices.

This superior performance stems from the well-orchestrated spin-channel-mediated reaction process, which is schematically recapitulated in Figure 6e: it encapsulates the sequential steps of CH_3SH activation at Cu sites, •H generation via S—H cleavage, and O_3 reduction at Mn sites enabled by the Cu—O—Mn electron relay. Figure 6f highlights a fundamental mechanistic divergence between $Cu_xMn_{3-x}O_4$ and conventional oxides. In traditional systems, O_3 and pollutant molecules compete for identical active sites, inevitably leading to incomplete oxidation and rapid catalyst deactivation—exemplified by the severe sulfur poisoning observed on Mn_3O_4. In stark contrast, $Cu_xMn_{3-x}O_4$ establishes clear functional division: Cu sites specialize in CH_3SH activation, while Mn sites selectively drive O_3 dissociation. These functionally distinct sites are interconnected by highly efficient spin channels, enabling rapid electron and radical exchange. This spatial and functional segregation not only eliminates competitive adsorption but also ensures continuous catalytic regeneration and deep CH_3SH mineralization—overcoming the persistent sulfur poisoning and kinetic limitations in conventional catalytic ozonation.

3 | Conclusion

In summary, we have demonstrated that engineering spin-polarized electron transfer pathways in $Cu_xMn_{3-x}O_4$ spinels can fundamentally transform the challenge of sulfur poisoning into a pollutant-driven, self-accelerating ozonation process. The optimized $Cu_{0.75}Mn_{2.25}O_4$ catalyst exhibits exceptional activity and stability, achieving complete mineralization of CH_3SH for over 28 h—a performance starkly contrasting with the rapid deactivation of undoped Mn_3O_4. By integrating in situ spectroscopy, kinetic analysis, and DFT calculations, we unveil a cooperative mechanism wherein Cu sites selectively cleave the S—H bond of CH_3SH to generate •H, which in turn trigger efficient O_3 activation at neighboring Mn sites via a barrierless reduction step, leading to rapid •OH production and deep oxidation of sulfur intermediates.

The superior efficiency originates from the establishment of efficient Cu—O—Mn spin channels, where Cu doping suppresses Jahn–Teller distortion, enhances O 2p—Mn 3d orbital hybridization, and creates a highly delocalized electron pathway that sustains rapid redox cycling between Cu^{2+}/Cu^{+} and Mn^{4+}/Mn^{3+} couples. This spin-channel-facilitated electron transfer not only accelerates ozone activation but also ensures instantaneous consumption of •H, thereby preventing the accumulation of sulfur-containing species and conferring remarkable anti-poisoning capability.

Beyond providing a high-performance, earth-abundant catalyst for sulfurous VOC removal, this work introduces a generalizable design principle: by tailoring spin-polarized metal–oxygen networks to relay pollutant-derived radicals, one can decouple catalytic activity from deactivation in advanced oxidation processes. This strategy opens a promising avenue for developing durable, energy-efficient catalytic systems for the sustainable abatement of reduced-sulfur and other challenging volatile pollutants under ambient conditions.

Acknowledgments

The authors acknowledge financial support from the National Natural Science Foundation of China (22476221, 22325607) and Guangdong Basic and Applied Basic Research Foundation (2022B1515020097). The authors thank PakGent Bioscience (Suzhou) Co., Ltd. for providing the

consumables (e.g., pipette tips), Ms. Wang Xin from Scientific Compass (www.shiyanjia.com) for providing ESR analysis, and Gao Bao from SCI-GO (www.sci-go.com) for performing XRD analysis.

Conflicts of Interest

The authors declare no conflicts of interest.

Data Availability Statement

The data that support the findings of this study are available from the corresponding author upon reasonable request.

References

1. I. Barnes, J. Hjorth, and N. Mihalopoulos, "Dimethyl Sulfide and Dimethyl Sulfoxide and Their Oxidation in the Atmosphere," *Chemical Reviews* 106 (2006): 940–975, https://doi.org/10.1021/cr020529.

2. M. O. Andreae and P. J. Crutzen, "Atmospheric Aerosols: Biogeochemical Sources and Role in Atmospheric Chemistry," *Science* 276 (1997): 1052–1058, https://doi.org/10.1126/science.276.5315.1052.

3. H. Huang, X. Xie, F. Xiao, et al., "A Critical Review of Deep Oxidation of Gaseous Volatile Organic Compounds via Aqueous Advanced Oxidation Processes," *Environmental Science & Technology* 58 (2024): 18456–18473, https://doi.org/10.1021/acs.est.4c07202.

4. T. M. Philipp, A. S. Scheller, N. Krafczyk, L. O. Klotz, and H. Steinbrenner, "Methanethiol: A Scent Mark of Dysregulated Sulfur Metabolism in Cancer," *Antioxidants* 12 (2023): 1780, https://doi.org/10.3390/antiox12091780.

5. D. Hanajima, K. Kuroda, K. Morishita, J. Fujita, K. Maeda, and R. Morioka, "Key Odor Components Responsible for the Impact on Olfactory Sense During Swine Feces Composting," *Bioresource Technology* 101 (2010): 2306–2310, https://doi.org/10.1016/j.biortech.2009.11.026.

6. D. He, J. Yu, Y. Mei, et al., "The Effects of Cr Addition in HZSM-5 on its Structure, Physicochemical and Catalytic Properties for Methyl Mercaptan Abatement," *Catalysis Communications* 112 (2018): 31–34, https://doi.org/10.1016/j.catcom.2018.04.013.

7. R. Zhang, J. Huang, M. Hu, et al., "Reinforcing Covalency via d–p–d Orbital Coupling Enables Dual-Site Selective Ozone Activation for Efficient CH_3SH Mineralization," *Environmental Science & Technology* 59 (2025): 26292–26302, https://doi.org/10.1021/acs.est.5c11499.

8. D. Ma, Q. Lian, Y. Zhang, et al., "Catalytic Ozonation Mechanism Over M_1-N_3C_1 Active Sites," *Nature Communications* 14 (2023): 7011, https://doi.org/10.1038/s41467-023-42853-8.

9. W. Qu, Z. Tang, S. Tang, et al., "Precisely Constructing Orbital Coupling-Modulated Iron Dinuclear Site for Enhanced Catalytic Ozonation Performance," *Proceedings National Academy of Science USA* 121 (2024): e2319119121, https://doi.org/10.1073/pnas.2319119121.

10. D. Ma, W. Liu, Y. Huang, D. Xia, Q. Lian, and C. He, "Enhanced Catalytic Ozonation for Eliminating CH_3SH via Stable and Circular Electronic Metal–Support Interactions of Si–O–Mn Bonds With Low Mn Loading," *Environmental Science & Technology* 56 (2022): 3678–3688, https://doi.org/10.1021/acs.est.1c07065.

11. W. Qu, T. Jin, K. Huang, et al., "Metal–Organic Frameworks-Driven Atomic Precision in Advanced Oxidation for Pollution Control," *Advanced Materials* 38 (2025): e12877, https://doi.org/10.1002/adma.202512877.

12. S. Lim, J. L. Shi, U. von Gunten, and D. L. McCurry, "Ozonation of Organic Compounds in Water and Wastewater: A Critical Review," *Water Research* 213 (2022): 118053, https://doi.org/10.1016/j.watres.2022.118053.

13. P.-J. Duan, J.-Y. Liu, L. Chen, et al., "Polymeric Products Deactivate Carbon-Based Catalysts in Catalytic Oxidation Reactions," *Nature Water* 3 (2025): 178–190, https://doi.org/10.1038/s44221-024-00377-5.

14. H. Li, J. Shang, Z. Yang, W. Shen, Z. Ai, and L. Zhang, "Oxygen Vacancy Associated Surface Fenton Chemistry: Surface Structure Dependent Hydroxyl Radicals Generation and Substrate Dependent Reactivity," *Environmental Science & Technology* 51 (2017): 5685–5694, https://doi.org/10.1021/acs.est.7b00040.

15. M. Huang, H.-Z. Liu, Q.-Q. Huang, et al., "Self-Activated Heterogeneous Fenton Process for Accelerated Degradation of Aromatic Pollutants Over Copper Oxide Catalysts," *Angewandte Chemie International Edition* 64 (2025): e202508754, https://doi.org/10.1002/anie.202508754.

16. M. Huang, Y. Han, W. Xiang, et al., "In Situ-Formed Phenoxyl Radical on the CuO Surface Triggers Efficient Persulfate Activation for Phenol Degradation," *Environmental Science & Technology* 55 (2021): 15361–15370, https://doi.org/10.1021/acs.est.1c03758.

17. X. Chen, W. Fu, H. Luo, et al., "Pollutant-Powered Oxygen Activation by Enzyme-Inspired Self-Sustaining Catalytic Membranes for Water Purification," *Angewandte Chemie International Edition* 65 (2025): e21747, https://doi.org/10.1002/anie.202521747.

18. J. Guo, Z. Gao, T. Zhang, L. Geng, and X. Xu, "Synergistic Dual-Single-Atom Catalysis Driving Auto-Catalytic Process Toward Oxidant-Free Fenton-Like Chemistry for Water Purification," *Angewandte Chemie International Edition* 65 (2025): e23480, https://doi.org/10.1002/anie.202523480.

19. L. Wang, Y. Wang, Z. Wang, et al., "Proton Transfer Triggered In-Situ Construction of C=N Active Site to Activate PMS for Efficient Autocatalytic Degradation of Low-Carbon Fatty Amine," *Water Research* 240 (2023): 120119, https://doi.org/10.1016/j.watres.2023.120119.

20. X. Zhou, G. Yang, Z. Zhou, et al., "Green Recovery of Precious Metals from E-waste via Autocatalytic Leaching," *Angewandte Chemie International Edition* 65 (2025): e23660, https://doi.org/10.1002/anie.202523660.

21. T. Tian, P. Zhu, C. He, Y. Xiong, J. Fang, and S. Tian, "Surface Mn-O_3* Complex-Mediated Nonradical Electron Transfer for Boosting Catalytic Ozonation of Organic Pollutants," *Applied Catalysis B: Environmental* 359 (2024): 124463, https://doi.org/10.1016/j.apcatb.2024.124463.

22. Y. He, J. Li, J. Tang, et al., "Constructed Electron-Dense Mn Sites in Nitrogen-Doped Mn_3O_4 for Efficient Catalytic Ozonation of Pyrazines: Degradation and Odor Elimination," *Water Research* 247 (2023): 120823, https://doi.org/10.1016/j.watres.2023.120823.

23. L. Y. Hao, Z. J. Tang, C. Y. Cai, et al., "Electron-Delocalized Cu^{2+} Activates Spin Channels in Spinel Oxides to Selectively Produce $^1O_2$ for Wastewater Treatment," *Angewandte Chemie International Edition* 64 (2025): e202504426, https://doi.org/10.1002/anie.202504426.

24. Y. Yang, J. Liu, F. Liu, Z. Wang, J. Ding, and H. Huang, "Reaction Mechanism for NH_3-SCR of NO_x Over $CuMn_2O_4$ Catalyst," *Chemical Engineering Journal* 361 (2019): 578–587, https://doi.org/10.1016/j.cej.2018.12.103.

25. X. Zhong, X. He, J. Tian, et al., "Acceleration of Molecular Oxygen Activation in m-Xylene Oxidation at Low-Temperature Through Building the Cu–O–Mn Electron Bridge," *Environmental Science & Technology* 59 (2025): 15468–15480, https://doi.org/10.1021/acs.est.5c04099.

26. R. Zhang, H. Zhou, T. Shao, et al., "High-Entropy Modulated High-Spin Localized Cobalt Sites Enhance Catalytic Ozonation for Efficient Odor Control," *Angewandte Chemie International Edition* 64 (2025): e202507109, https://doi.org/10.1002/anie.202507109.

27. J. Yang, Y. Huang, Y. Chen, et al., "Active Site-Directed Tandem Catalysis on CuO/V_O-MnO_2 for Efficient and Stable Catalytic Ozonation of S-VOCs Under Mild Condition," *Nano Today* 35 (2020): 100944, https://doi.org/10.1016/j.nantod.2020.100944.

28. Y. Li, J. Qu, F. Gao, et al., "In Situ Fabrication of Mn_3O_4 Decorated Graphene Oxide as a Synergistic Catalyst for Degradation of Methylene Blue," *Applied Catalysis B: Environmental* 162 (2015): 268–274, https://doi.org/10.1016/j.apcatb.2014.06.058.

29. S. P. Varghese, B. Babu, R. Prasannachandran, R. Antony, and M. M. Shaijumon, "Enhanced Electrochemical Properties of Mn_3O_4/Graphene Nanocomposite as Efficient Anode Material for Lithium Ion Batteries,"

Journal of Alloys and Compounds 780 (2019): 588–596, https://doi.org/10.1016/j.jallcom.2018.11.394.

30. F. Wang, M. Xiao, X. Ma, S. Wu, M. Ge, and X. Yu, "Insights Into the Transformations of Mn Species for Peroxymonosulfate Activation by Tuning the Mn_3O_4 Shapes," *Chemical Engineering Journal* 404 (2021): 127097, https://doi.org/10.1016/j.cej.2020.127097.

31. Y. Zhang, Z. Zeng, Y. Li, Y. Hou, J. Hu, and Z. Huang, "Effect of the A-Site Cation Over Spinel AMn_2O_4 (A = Cu^{2+}, Ni^{2+}, Zn^{2+}) for Toluene Combustion: Enhancement of the Synergy and the Oxygen Activation Ability," *Fuel* 288 (2021): 119700, https://doi.org/10.1016/j.fuel.2020.119700.

32. J. Zhang, Z. Wang, X. Lin, et al., "Mn−Ce Symbiosis: Nanozymes with Multiple Active Sites Facilitate Scavenging of Reactive Oxygen Species (ROS) Based on Electron Transfer and Confinement Anchoring," *Angewandte Chemie International Edition* 64 (2025): e202416686, https://doi.org/10.1002/anie.202416686.

33. S.-M. Hao, J. Qu, Z.-S. Zhu, X.-Y. Zhang, Q.-Q. Wang, and Z.-Z. Yu, "Hollow Manganese Silicate Nanotubes with Tunable Secondary Nanostructures as Excellent Fenton-Type Catalysts for Dye Decomposition at Ambient Temperature," *Advanced Functional Materials* 26 (2016): 7334–7342, https://doi.org/10.1002/adfm.201603315.

34. C. Shan, Y. Zhang, Q. Zhao, et al., "Acid Etching-Induced In Situ Growth of λ-MnO_2 Over CoMn Spinel for Low-Temperature Volatile Organic Compound Oxidation," *Environmental Science & Technology* 56 (2022): 10381–10390, https://doi.org/10.1021/acs.est.2c02483.

35. Y. Li, T. Chen, S. Zhao, et al., "Engineering Cobalt Oxide With Coexisting Cobalt Defects and Oxygen Vacancies for Enhanced Catalytic Oxidation of Toluene," *ACS Catalysis* 12 (2022): 4906–4917, https://doi.org/10.1021/acscatal.2c00296.

36. P. Xu, S. Luo, J. Liang, D. Pan, B. Zou, and J. Li, "High-Performance 2.2 V Asymmetric Supercapacitors Achieved by Appropriate Charge Matching between Ultrahigh Mass-Loading Mn_3O_4 and Sodium-Jarosite Derived FeOOH," *Advanced Functional Materials* 34 (2024): 2313927, https://doi.org/10.1002/adfm.202313927.

37. H.-L. Han, L. Fu, and Y.-P. Lee, "Infrared Spectrum of Mass-Selected CH_3S Radicals Investigated With Infrared + Vacuum Ultraviolet Photoionization," *Chemical Physics Letters* 515 (2011): 1–6, https://doi.org/10.1016/j.cplett.2011.06.090.

38. W. Qu, Z. Tang, S. Tang, et al., "Cation Substitution Induced d-Band Center Modulation on Cobalt-Based Spinel Oxides for Catalytic Ozonation," *Advanced Functional Materials* 33 (2023): 2301677, https://doi.org/10.1002/adfm.202301677.

39. Y. Mu, X. Tong, Y. Guan, et al., "Simultaneous Copper and EDTA Ligands Recovery From Electroless Effluent With Metallic Copper and Formaldehyde," *Environmental Science & Technology* 59 (2024): 968–977, https://doi.org/10.1021/acs.est.4c09970.

40. Y. Qi, Y. Yang, X. Yu, et al., "Unveiling the Contribution of Hydrogen Radicals to Per- and Polyfluoroalkyl Substances (PFASs) Defluorination: Applicability and Degradation Mechanisms," *Environmental Science & Technology* 59 (2025): 1875–1886, https://doi.org/10.1021/acs.est.4c10411.

41. X. Feng, J. Liu, L. Chen, et al., "Hydrogen Radical-Induced Electrocatalytic N_2 Reduction at a Low Potential," *Journal of the American Chemical Society* 145 (2023): 10259–10267, https://doi.org/10.1021/jacs.3c01319.

42. Z. Chen, C. Li, J. Gao, et al., "Efficient Reductive Destruction of Perfluoroalkyl Substances Under Self-Assembled Micelle Confinement," *Environmental Science & Technology* 54 (2020): 5178–5185, https://doi.org/10.1021/acs.est.9b06599.

43. S. Mu, H. Lu, Q. Wu, et al., "Hydroxyl Radicals Dominate Reoxidation of Oxide-Derived Cu in Electrochemical CO_2 Reduction," *Nature Communications* 13 (2022): 3694, https://doi.org/10.1038/s41467-022-31498-8.

44. C. He, Y. Wang, Z. Li, et al., "Facet Engineered α-MnO_2 for Efficient Catalytic Ozonation of Odor CH_3SH: Oxygen Vacancy-Induced Active Centers and Catalytic Mechanism," *Environmental Science & Technology* 54 (2020): 12771–12783, https://doi.org/10.1021/acs.est.0c05235.

45. Y. Huang, D. Ma, W. Liu, et al., "Enhanced Catalytic Ozonation for Eliminating CH_3SH via Graphene-Supported Positively Charged Atomic Pt Undergoing Pt^{2+}/Pt^{4+} Redox Cycle," *Environmental Science & Technology* 55 (2021): 16723–16734, https://doi.org/10.1021/acs.est.1c06938.

46. D. Ma, J. Cao, K. Liu, et al., "Interstitial Carbon-Platinum Electronic Metal-Support Interaction Structure Boost Synergistic Removal of O_3 and CH_3SH via Surface Atomic Oxygen," *Applied Catalysis B: Environmental* 329 (2023): 122578, https://doi.org/10.1016/j.apcatb.2023.122578.

47. S. Tang, T. Zhong, Z. Yao, et al., "Construction of Spatially Adjacent Ni and Co-Based Spinel Frustrated Lewis Pair Sites for Efficient Catalytic Ozonation," *Small* 21 (2025): 2500310, https://doi.org/10.1002/smll.202500310.

Supporting Information

Additional supporting information can be found online in the Supporting Information section.

Supporting File 1: anie71810-sup-0001-SuppMat.pdf.